Tin Telluride Quantum Dots as a Novel Saturable Absorber for Q-switching and Mode locking in Fiber Lasers

Safayet Ahmed [1,2,†], *Junpeng Qiao* [1,2,4†], *Ping Kwong Cheng* [1,2,†], *Ahmed Mortuza Saleque* [1,2], *Mohammad Ismail Hossain* [1,2,3], *Long-Hui Zeng* [1,2], *Jia Zhao* [4], *Wayesh Qarony* [1,2], *Yuen Hong Tsang* [1,2,*]

[1]Department of Applied Physics and Materials Research Center, The Hong Kong Polytechnic University, Hung Hom, Kowloon, Hong Kong

[2]Shenzhen Research Institute, The Hong Kong Polytechnic University, 518057 Shenzhen, Guangdong, People's Republic of China.

[3]Department of Materials Science and Engineering, City University of Hong Kong, Hong Kong

[4]School of Information Science and Engineering, Shandong University, Qingdao 266237, China

†Safayet Ahmed, Junpeng Qiao and Ping Kwong Cheng contributed equally to this work

*Corresponding author: E-mail: yuen.tsang@polyu.edu.hk

Abstract

Tin telluride (SnTe) quantum dots (QDs) have attracted considerable interest in the optoelectronic field owing to their favorable properties over conventional QDs, such as a relatively large Bohr radius (95 nm) and low toxicity level. However, till date, the nonlinear optical (NLO) properties and ultrafast photonics applications of SnTe QDs have remained unexplored. In this study, SnTe QDs with an average diameter of 74 nm (smaller than the Bohr radius of SnTe) are fabricated via a liquid-phase exfoliation method. Consequently, the nonlinear saturable absorption properties of such SnTe QDs are explored by realizing a modulation depth of 2.2% and saturable intensity of 1.67 GW/cm^2. The prepared QDs are then utilized as saturable absorber (SA) in the Erbium-doped fiber laser ring cavity system. Moreover, Q-switched, and mode-locked laser pulses with a pulse width of 1.81 μs and 691 fs are generated, respectively. Harmonic mode-locking with a high

repetition rate of 62.1 MHz (fifth-order) is experimentally realized. This is the first demonstration, to our knowledge, of utilizing SnTe QDs-SA for generating ultrafast laser pulses along with high-repetition-rate harmonic mode-locking pulses. Therefore, this study will establish a new research scope for SnTe QDs in ultrafast photonics, nonlinear photonics, frequency combs, and optical communications.

Keywords: Quantum dots; SnTe-QDs; Saturable absorber; Q-switching; Mode locking, Harmonic mode-locking.

1. Introduction

Two-dimensional (2D) quantum dots (QDs) are structurally tailored components of standard 2D materials and have acquired widespread interest in the scientific community owing to their attractive and unique optoelectronic properties.[1,2] In QDs, inorganic semiconducting nanocrystallites exhibit nanometer-sized excitons, and the critical dimensions of such excitons are smaller or equivalent to the size of the Bohr radius of excitons.[3] Owing to the extremely small size of QDs, quantum confinement occurs in the electrons and holes from all three dimensions, leading to a higher surface-to-volume ratio and stronger edge effect.[4] This not only results in remarkable structural transformations but also influences the spacing of energy levels and discrete electronic states, thereby increasing the effective bandgap of the material. For these reasons, two-dimensional (2D) material-based QDs have demonstrated exceptional properties and are employed in a wide range of applications such as in solar cells, photodetectors, supercapacitors, telecommunications, optical sensors, and laser systems.[5–7] In comparison to 2D nanosheets, 2D QDs have higher solubility, doping ease, better photochemical stability and demonstrate nonlinear

optical effects.[8] Such advantageous phenomena of 2D QDs have already been demonstrated by Hui et al., wherein WS_2 QDs exhibited superior nonlinear optical absorption (NOA) properties compared with those of nanosheets. The reason behind this superior property was the decrease in the NOA onset threshold and the optical limiting threshold due to the reduction in size and thickness of the material. [9] Similarly, Xu et al. reported that QDs had better saturable absorption properties owing to their lower saturable intensity compared to bulk materials. [10] Therefore, 2D QDs can be considered as a credible choice for saturable absorber (SA) materials that reduce the optical absorption as the intensity of the incident light increases. The features of such SAs make it possible to induce passive Q-switching, mode-locking, and harmonic mode-locking (HML) techniques and generate short to ultrashort laser pulses with a higher energy, power, and repetition rate (RR). The produced pulses can be further utilized in various applications such as in optical fiber communication, product storage, fiber sensing, and medical diagnosis. [11–14]

Till date, several QDs have been used as SAs in the laser cavity, which produces ultrafast laser pulses by inducing Q-switching and mode-locking operations. Previously, black phosphorus and graphene QDs were used as NLO materials, and they demonstrated better performance than nanosheets.[15–18] Shi et al. and Zang et al. observed the SA property of $NbSe_2$ and GaTe QDs by demonstrating the generation of ultrafast laser pulses in both Er-doped and Yb-doped laser cavity, respectively.[19,20] Recently, QDs based on group II–VI chalcogenides (cadmium sulfide, CdS; cadmium selenide, CdSe) and group IV–VI chalcogenides (lead sulfide, PbS) have been introduced as SAs in the fiber laser system, and the generation of ultrafast laser pulses has been demonstrated.[21–23] However, Pb- and Cd-based QDs are toxic heavy metals that might pose significant risks to the environment.[24] Therefore, low-toxicity QDs are gaining considerable scientific and technological interest.

Recently, Sn chalcogenides (SnX, X = S, Se, Te) have been recommended as a promising alternative to Pb and Cd chalcogenides owing to their relatively low toxicity and high abundance.[25] Among different SnX materials, bulk SnTe is a narrow-bandgap semiconductor material that exhibits various characteristics such as a direct bandgap (0.18 eV, bulk), high dielectric constant ($\epsilon_\infty \approx 45$), thermal stability,[26–28] and cubic rock-salt crystal structure with numerous symmetry surfaces.[29,30] Moreover, as SnTe has a larger Bohr radius (95 nm) and small effective electron–hole mass ($m_{eh} \approx 0.025m_0$),[31] the properties of SnTe nanoparticles can be tuned within the quantum confinement region by changing its size only, which might be difficult for conventional QDs with smaller Bohr radii, such as carbon-QDs (less than 10 nm), CdSe (6.1 nm), CdS (3.4 nm), and PbS (20 nm).[3,32–34] However, till date, only a few works have been practically demonstrated using SnTe QDs. Ghandomani et al. illustrated the capability of SnTe QDs in a QD solar cell device, working in the visible-near infrared regions.[35] Additionally, Cryer et al. and Yang et al. established mid-infrared (MIR) detection beyond 3 μm, allowing for achieving a high-performance photodetector working in a broadband wavelength ranging from deep ultraviolet (UV) to the MIR region with high responsivity, by using SnTe QDs and nanoparticles.[36,37] Although few studies revealed that Sn chalcogenides (SnS,[39] SnSe[40]) are good nonlinear materials, no studies have been presented till date regarding the NLO properties as well as saturable absorption performance of SnTe QDs or other Sn chalcogenides based QDs.

To the best of our knowledge, this is the first demonstration of utilizing SnTe QDs as an effective SA in an erbium-doped fiber laser (EDFL) ring cavity system. Achieving passive Q-switching, mode-locking, and HML operations have led to our proposed system being superior to other recent works. For Q-switching and mode-locking operations, the prepared QDs-SA facilitated the generation of laser pulses with a pulse width of 1.81 μs and 691 fs, respectively. In

addition,, HML pulses were achieved with a high RR of 62.1 MHz (fifth-order) by tuning the pump power and inter-cavity polarization. Hence, our study will inspire researchers for the novel application of SnTe QDs in ultrafast photonics, nonlinear photonics, optical metrology, and optical communication.

2. Sample preparation and characterization:

2.1 SnTe QDs fabrication via liquid-phase exfoliation

In this study, SnTe QDs were fabricated by employing a low-cost liquid-phase exfoliation (LPE) process on SnTe powder (Six carbon Inc.). The powder was synthesized by the chemical vapor transport method, where Sn and Te were sealed under a high vacuum, followed by high temperature (800 °C) to form SnTe powder. Isopropyl alcohol (IPA) was used as a solvent owing to its low boiling points and low cost compared with other solvents.[41] The powder was initially mixed with IPA at a ratio of 2 mg/mL. The mixture was then ultrasonicated for 24 h at 400 W output power and 40 kHz frequency to obtain the SnTe QDs. The temperature was maintained at approximately 23 °C to avoid powder degradation. Subsequently, SnTe QDs with the IPA solution were centrifuged (Zonkia HC-3018) for 5 min at 2000 rpm to ensure that the supernatant of the mixture did not contain any unexfoliated powder or bulk impurities. The supernatant was collected and drop-casted on the quartz substrate. Then, it was dried over a hot plate at 80 °C and subsequently retained for further characterization. The complete procedure of SnTe QD fabrication is demonstrated in **Figure 1(a).**

2.2. Physical characteristics of SnTe nanosheets

In this section, the physical characteristics of SnTe QDs are presented. Figure 1(b) shows a

standard unit cell of cubic phase β-SnTe (lattice parameter, a = 6.42 Å). The SnTe crystal structure consists of Sn and Te, both of which crystallize to form a three-dimensional (3D) checkerboard pattern in interpenetrating FCC sublattices. Generally, bulk SnTe crystallizes in a rock-salt crystal structure (FCC) with a space group of $Fm\bar{3}m$ (225) under ambient conditions.[29] To determine the crystal structure, the X-ray diffraction (XRD) pattern (Rigaku SmartLab 9kW – Advance) of SnTe powder was observed, as shown in Figure 1(c) (top). The locations of the diffraction peaks were detected at 2θ = 28°, 40°, 49°, 58°, 66°, 73°, and 87°, corresponding to the planes of (200), (220), (222), (400), (420), (422), and (440) planes. These peaks are well matched with the peaks of SnTe ($Fm\bar{3}m$, 225, 00-046-1210) cubic crystal structure (Figure 1(c), bottom).[29] In addition, two small peaks observed at 2θ = 27° and 38° are the peaks of the quartz substrate. A scanning electron microscopy (SEM, TESCAN VEGA3) picture of SnTe powder is provided in Figure S1. Furthermore, the chemical composition of the raw SnTe powder was verified by X-ray photoelectron spectroscopy (XPS, Thermo Scientific Nexsa). In the XPS results, the core-level regions of Sn_{3d} (Figure 1(d)) and Te_{3d} (Figure 1(e)) are demonstrated. The peaks at 486 and 495 eV correspond to the $Sn_{3d5/2}$ and $Sn_{3d3/2}$ spin doublet characteristics from Sn^{2+}, respectively. For Te^{2-}, the characteristics of the $Te_{3d5/2}$ and $Te_{3d3/2}$ peaks are positioned at 572 and 583 eV, respectively. These results are in agreement with the previously mentioned results for SnTe materials.[42] Moreover, from the XPS data, the atomic ratios of Sn and Te are observed to be 51% and 49%, respectively. As the ratio of the elements are close to 1:1, no possible defects are identified in the sample.

After exfoliation, the size of the fabricated SnTe QDs is determined by utilizing a field emission scanning electron microscope (FESEM, TESCAN MAIA3). Figure 2(a) shows that the prepared samples are uniformly distributed. After analyzing the 369 flakes shown in the FESEM image, the

average lateral size of the QDs along the short axis was observed to be 74 nm (Figure S2(a)) and along the long axis to be 77 nm (Figure S2(b)). As mentioned earlier, when the dimension of nanoparticles is less than their Bohr radius, the particle can be defined as QDs.[3,43] As the Bohr radius of SnTe particles is 95 nm, and the size of the majority of as-prepared SnTe nanoparticles is less than the Bohr radius, these prepared particles can be recognized as QDs. For further investigation, atomic force microscopy (AFM, Asylum MFP 3D Infinity) was used to examine the surface roughness and thickness of the as-prepared QDs (Figure 2(b)). The height profiles of randomly selected flakes (denoted by Lines 1, 2, and 3 in the AFM image) are shown in Figure 2(d), (e), and (f), respectively. The AFM images showed that the thickness of the flakes is approximately 5.2 nm (line 1), 5.3 nm (line 2), and 5.8 nm (line 3). The lateral size of the selected flakes was 65 nm (line 1), 70 nm (line 2), and 80 nm (line 3), in agreement with the FESEM results. Moreover, the height profile of the prepared nanosheets over a 2 μm area was analyzed from the 3D AFM image (Figure S2 (c)). Figure S2(d) shows that the thickness of the majority of the as-prepared QDs is approximately 6 nm. Therefore, it can be concluded that the prepared QDs are ultrathin and are in good agreement with the morphological features provided in the transmission electron microscopy (TEM) image.

Later, the SnTe QD samples were characterized using a field emission electron microscope (STEM, JEOL Model JEM-2100F). In Figure 2(c), the TEM image of SnTe QDs is shown, which was acquired at a 30k magnification. The size of the QD is in accordance with the size of the QDs mentioned in the FESEM image. Moreover, the high-resolution TEM (HRTEM) images of randomly selected areas are shown in Figure 2(g), where three different diffraction patterns (denoted with yellow, white, and green boxes), with interplanar spacings of 0.322 nm, 0.229 nm, and 0.188 nm, respectively. These three planes are well matched with the (200), (220), and (222)

planes of a cubic SnTe structure. In addition, the selected area electron diffraction pattern was determined to characterize the crystallinity of the fabricated SnTe QDs. Figure 2(h) shows interplanar spacings from the center transmission spots to the three selected diffraction spots, which are 0.327, 0.232 nm, and 0.188 nm, corresponding to the (200), (220), and (222) planes, respectively (matched with JCPDS card no. 00-046-1210[29] and supports the XRD results). Subsequently, the electron-dispersive X-ray spectroscopy (EDS) profile of the as-prepared sample was observed, as shown in Figure 2(i), where it is confirmed that the samples do not contain any impurities, and the major peaks belong to Tin (Sn) and Telluride (Te). As a copper (Cu) grid was employed as the substrate during STEM measurement, some Cu signals were present in the EDS profile. From these phenomena, it can be determined that the prepared QDs indeed belong to the cubic SnTe materials.

Raman spectroscopy is the most commonly used non-destructive method for realizing the structures and vibrational modes of nanomaterials; hence, the Raman spectrum (WITEC Confocal Raman system) of SnTe materials was determined using a 532 nm excitation laser with a 1.0 mW power, as depicted in Figure 3(a). As for the SnTe powder, three Raman peaks are observed (bottom, Figure 3(a)). The peak at 113 cm^{-1} is assigned to the longitudinal optical (LO) mode of symmetry, A_1. The other two peaks situated at 85 cm^{-1} and 134 cm^{-1} are attributed to the transverse optical (TO) mode of symmetry, E. The former TO peak might have occurred due to low-energy scattering. These results are consistent with the earlier reported work on SnTe materials.[44] As described earlier, the size of the SnTe materials decreases to the order of nanometers and produces QDs. Owing to this phenomenon, in-plane vibration stiffnesses occur in the as-prepared samples, causing a blue shift in the two E (TO) and one A_1 (LO) Raman peaks at 5 cm^{-1}, 4 $cm^{-1,}$ and 5 cm^{-1}, respectively, as shown in Figure 3(a) (Top). The blue shift of the Raman peaks resembles the

characteristics of other QDs.[45] In addition, the UV–VIS–NIR (Perkin Elmer) spectra of the SnTe QDs is shown in Figure 3(b), confirming that SnTe QDs are appropriate for visible to mid-infrared region applications. The bandgap of the prepared QDs was further evaluated from the absorbance spectra using the Tauc plot method. Figure 3(c) shows that the bandgap of the sample is 0.74 eV (larger than the bulk material), indicating that the prepared QDs are suitable for absorption in the 1.55 μm range. It is noted that, the bandgap increases due to the electron confinement in QDs (quantum size effect), which occurs when the size of the particle decreases beyond the Bohr radius.[46]

3. Ultrafast photonics applications

3.1. Nonlinear optical characterization

A balanced twin-detector method was employed to determine the nonlinear saturable absorption property of the SnTe QDs-SA.[47] First, a side-polished fiber (SPF) was selected to allow the interaction between the light traveled within the fiber and the SnTe QDs. By dropping SnTe QDs–IPA solution on the SPF for a few times, SnTe QD-based SPF-SA was prepared. Subsequently, a homemade ultrafast laser source with a 2.1 ps pulse width (center wavelength at 1560 nm) and a 15.04 MHz pulse RR was utilized for initiating the investigation. The detection system along with the nonlinear saturable absorption curve is shown in Figure 4. The obtained experimental results are denoted with blue balls, and the fitted curve is indicated by a solid red line in Figure 4(b). Here, the fitted curve is constructed using Equation (1). From the curve, the modulation depth and the saturable intensity of SnTe QDs-based SA are determined to be approximately 2.2% and 1.67 GW/cm^2, respectively. Therefore, it could be concluded that SnTe QDs-SA has good NLO properties and can be utilized for the generation of ultrafast laser pulses.

$$T(I) = 1 - \Delta T * \exp\left(\frac{I}{I_{sat}}\right) - T_{ns} \quad \textbf{(1)}$$

Here, T(I), I_{sat}, ΔT, and T_{ns} denote the transmittance, saturable intensity, modulation depth, and non-saturation loss, respectively. The calculation process of nonlinear curve determination is provided in the supporting documents.

3.2. Schematic of fiber laser system

A ring cavity structure-based fiber laser system (Figure 5(a)) was developed with a 0.7 m long erbium-doped fiber (EDF, LIEKKI Er 110-4/125) and a 11.66 m long single-mode fiber (SMF-28), with a group velocity dispersion of 12 $ps^2\ km^{-1}$ and -19 $ps^2\ km^{-1}$, respectively. For the pumping equipment, a 976 nm laser diode was connected with the EDF through a 980/1550 nm wavelength division multiplexer (WDM). Moreover, a polarization-independent isolator (PI-ISO) was incorporated into the laser cavity to maintain the direction of the propagated light. To fine-tune the intracavity birefringence and the polarization state, a three-paddle polarization controller (PC) was adopted. Here, SnTe QD-based SA was utilized in the polished region of the SPF that interacts with the evanescent waveguide provided by the SPF. Thus, a nonlinear optical absorption phenomenon was achieved. The insertion loss and the polarization-dependent loss (PDL) of the prepared SA were measured to be approximately 5.93 dB and 1.61 dB, respectively. The results for the ultrafast laser pulses were detected using a 10% optical coupler connected to a 400 MHz oscilloscope (WaveRunner 44MXi, LeCroy) combined with a photodetector (DET01CFC, ThorLabs). The spectrum of the ultrafast pulses was analyzed using an optical spectrum analyzer (AQ6370B, Yokogawa). An autocorrelator (FR-103XL, Femtochrome) was employed to measure the pulse width of the mode-locked pulse. The total cavity length was measured to be approximately 12.4 m, which facilitated the enhancement of the pulse quality.

3.3. Passive Q-switching operation

Owing to its usability in applications such as nonlinear optics, industrial laser engraving, eye surgery, and skin treatment, Q-switched laser pulses have received considerable attention in the research field.[48–50] In our laser system, a stable Q-switched pulse train was detected for a specific polarization, as the pump power of the 976 nm pumping diode reached 66.16 mW (threshold level). Figure 5(b) shows that as the pump power is regulated from 66.16 to 354.36 mW, the output power and the single pulse energy increased from 3.73 to 126.02 μW (black dots/line) and 0.237 to 2.18 nJ (blue dots/line), respectively. For a similar range of pump power alternation, the pulse RR is increased from 15.72 to 57.84 kHz, and the full width at half maximum (FWHM) of the pulse duration is decreased from 20.57 to 1.81 μs, as illustrated in Figure 5(c). Moreover, from the single pulse profile shown in Figure 5 (d), it can be verified that for the maximum pump power of 354.36 mW, the obtained pulse width is 1.81 μs, which is one of the narrowest pulse widths attained relative to the different Q-switched pulse laser systems, as mentioned in **Table 1**. Additionally, from the pulse train shown in Figure 5 (e) (inset is a larger scale), it can be understood that the Q-switched pulse is very stable. The stability can be further verified by the value of the signal-to-noise ratio (SNR), which is calculated up to 51 dB from the radio-frequency (RF) spectrum (resolution bandwidth of 76.5 Hz), as shown in Figure 5(f). Finally, the central wavelength of the Q-switched operation was recorded at 1566 nm, as shown in Figure 5(g).

3.4. Passive mode-locking and harmonic mode-locking pulse generation

In addition to the Q-switching feature, the mode-locking operation for ultrashort laser pulse generation is another major application of SAs. Herein, the potential of SnTe QD SA is explored further in this area. In our EDFL system, a stable mode-locking operation with a fundamental RR of 12.41 MHz was accomplished by changing the pump power beyond the threshold value of 73.59 mW and adjusting the polarization along with the intracavity birefringence using a PC. In Figure 6(a), it is demonstrated that while the pump power is regulated from 73.59 to 385.353 mW by keeping the three paddles of PC in a specific angle (Figure S3(a)), the corresponding output power of the mode-locked pulse is improved from 0.185 to 2.603 mW. Moreover, by using the intensity autocorrelator, the FWHM pulse width of the mode-locked pulse was measured as 1.066 ps. Subsequently, by using the sech^2 profile, the autocorrelation trace was fitted, and a real pulse width of 691 fs was obtained (Figure 6(b)). Table 2 shows that the pulse width attained herein is comparable to most 2D materials and QD-based SAs. From Figure 6(c), a stable mode-locking pulse train with a 80.6 ns pulse-to-pulse interval can be observed at a pump power of 354 mW. This pulse interval value is in correspondence with the cavity length of 12.4 m, which further proves that the generated pulse is due to the mode-locking mechanism. The stability of the generated pulses can be determined from the pulse train envelope shown in Figure 6(d) (actual oscilloscope picture for 1 μs/div, is shown in Figure S3(b)). Moreover, from the RF spectrum of the mode-locked pulse, shown in Figure 6(e), it can be determined that the primary peak is located at an RR of 12.41 MHz with an SNR of approximately 52 dB (resolution bandwidth of 7.3 kHz), further indicating the stability of the obtained pulse. Subsequently, for further analysis of the signal quality, the RF spectrum was observed with a span of 100 MHz (inset of Figure 6(e)), and the spacing of the signal peak is observed to be 12.41 MHz, which is in agreement with the fundamental RR. From Figure 6(f), the wavelength spectrum, centered at 1562.05 nm and having

an FWHM bandwidth of 4.23 nm, can be determined. Additionally, in the inset, the wavelength spectrum over a 5 h period is provided, from where it can be observed that there is no optical spectrum drift, which further proves the constancy of the mode-lock operation. Finally, the time–bandwidth product (TBP) was determined to be 0.359, which is marginally greater than the theoretical transformation limit value of 0.315, suggesting a slight chirping of the mode-locked pulses.

The addition of an adequately high nonlinear effect in the laser cavity can produce HML pulses that are useful in many areas, such as optical communications, frequency bandages, and biomedical research.[51] Different methods can be utilized to attain HML pulses, such as increasing the single-mode fiber length, regulating the pump power, adjusting the polarization, and introducing excellent nonlinear optical materials.[52] Herein, by changing the polarization with PC as well as retaining the pump power at the highest level (385.353 mW) and implementing SnTe QDs as a nonlinear optical material, second-, third-, and fifth-order HML pulses are obtained. The pulse trains of these HML pulses for a span of 500 ns are shown in Figure 7(a), (b), and (c), respectively. The figures show that for the harmonic pulse trains, the pulse-to-pulse interval for two, three, and five consecutive pulses are 80.6 ns, which are comparable to the fundamental signal. This confirms the successful generation of HML. Moreover, the RF spectrum at 24.82 MHz (second-order harmonic), 37.2 MHz (third-order harmonic), and 62.1 MHz (fifth-order harmonic) are provided in Figure S4 & Figure 7(d), respectively. Furthermore, the SNR values of the harmonic pulse trains are measured to be 48 dB, indicating that the signals are stable during harmonic pulse generation; the super-mode suppression ratio for the HML is as high as 48 dB. Finally, the wave spectrum of the fifth-order HML pulse with a central wavelength of 1562.4 nm and a 3 dB bandwidth of 1.66 nm can be observed from the inset of Figure 7(d). HML is caused

by the strong nonlinearity of the SA material. Hence, the production of SnTe QDs enhances the NLO properties of the material and allows for the initiation of HML inside the laser cavity, which would motivate those interested to perform further research with the SnTe QDs.

In Figure S5, the saturable absorption mechanism of SnTe is interpreted by the Pauli-blocking principle.[53] Under low excitation intensity, when the excitation photon energy is larger than the bandgap energy (ΔE), an electron from the valence band (red part) can absorb a photon and gets excited to the conduction band (blue part). Then, the distribution of hot electrons rapidly thermalizes and cools down to form a hot Fermi–Dirac distribution. In this state, the newly generated electron–hole pairs would hold the position and block the absorption of the photons around energy (+E/2). Hence, an electron–hole equilibrium state is established. However, when the excitation intensity reaches a relatively high level, the photocarriers will instantaneously increase and occupy the energy states near the edge of the valence and conduction band instantly. As a result, owing to the Pauli-blocking principle, the absorption will be blocked. Eventually, the photons can transparently transmit through the SnTe QDs without absorption, ensuring the saturation of the sample.

5. Conclusion

In this study, SnTe QDs were fabricated using the LPE method. Several material characterizations were performed to analyze the crystal structure, chemical composition, size, thickness, lattice spacing, absorbance, and bandgap of the prepared sample. The nonlinearity of the fabricated QDs was determined by the twin detector method. The modulation depth and saturation intensity were realized to be 2.2% and 1.67 GW/cm^2, respectively. Next, by integrating the SnTe QDs as an SPF-based SA in an EDFL ring cavity system, Q-switching and mode-locking operations along with

HML up to the fifth order were observed. In the Q-switched state, the minimum pulse width and maximum single pulse energy were determined to be 1.81 μs and 2.18 nJ, respectively, with a center wavelength of 1566 nm. For the mode-locking operation, a pulse of 691 fs pulse width was realized at a center wavelength of 1562.05 nm. In addition, the maximum output power of 2.603 mW and SNR of 52 dB were determined. By monitoring the wavelength spectrum for nearly 5 h, the stability of the mode-locking operation was determined. Finally, by increasing the pump power and adjusting the polarization, HML (fifth-order) pulses up to 62.1 MHz RR was obtained. These results of attaining Q-switching, mode-locking, and HML together indicate that SnTe QDs have admirable NLO and saturable absorption properties. Hence, this study will open new possibilities of SnTe QDs for the advancement of ultrafast photonic devices, nonlinear photonics, and communication applications.

Supporting Information

Supporting Information is available from the Wiley Online Library or from the author.

Conflicts of interest

There is no conflict to declare.

Acknowledgments

This work is financially supported by the Research Grants Council of Hong Kong, China (Project number: 152093/18E); the Hong Kong Polytechnic University Shenzhen Research Institute, Shenzhen, China (Grant Code: the science and technology innovation commission of Shenzhen (JCY20180306173805740)); Hong Kong Scholars Program (XJ2019020); N.B. acknowledges the financial support by the UCONN's Office of the Vice President for Research (OVPR) through the Research Excellence Program (REP).

Received: ((will be filled in by the editorial staff))
Revised: ((will be filled in by the editorial staff))
Published online: ((will be filled in by the editorial staff))

Reference

[1] A. Zunger, *Phys. Status Solidi Basic Res.* **2001**, *224*, 727.

[2] A. Franceschetti, H. Fu, L. W. Wang, A. Zunger, *Phys. Rev. B* 1999, *60*, 1819.

[3] T. Archana, K. Vijayakumar, G. Subashini, A. Nirmala Grace, M. Arivanandhan, R. Jayavel, *RSC Adv.* **2020**, *10*, 14837.

[4] A. Manikandan, Y. Z. Chen, C. C. Shen, C. W. Sher, H. C. Kuo, Y. L. Chueh, *Prog. Quantum Electron.* **2019**, *68*, 100226.

[5] J. M. Baruah, J. Narayan, *J. Opt.* **2018**, *47*, 202.

[6] H. Kaur, H. S. Bhatti, K. Singh, *J. Mater. Sci. Mater. Electron.* **2019**, *30*, 2246.

[7] K. P. Musselman, K. H. Ibrahim, M. Yavuz, *APL Mater.* 2018, *6*, 120701.

[8] H. Long, L. Tao, C. P. Chiu, C. Y. Tang, K. H. Fung, Y. Chai, Y. H. Tsang, *Nanotechnology* **2016**, *27*, 414005.

[9] H. Long, L. Tao, C. Y. Tang, B. Zhou, Y. Zhao, L. Zeng, S. F. Yu, S. P. Lau, Y. Chai, Y. H. Tsang, *Nanoscale* **2015**, *7*, 17771.

[10] Y. Xu, Z. Wang, Z. Guo, H. Huang, Q. Xiao, H. Zhang, X. F. Yu, *Adv. Opt. Mater.* **2016**, *4*, 1223.

[11] M. E. Fermann, I. Hartl, *Nat. Photonics* **2013**, *7*, 868.

[12] C. Xu, F. W. Wise, *Nat. Photonics* **2013**, *7*, 875.

[13] Y. Chen, Y. Lin, Y. Zou, Z. Luo, Y. Huang, *J. Light. Technol* **2012**, *20*, 9940.

[14] Z. Wang, C. Li, J. Ye, Z. Wang, Y. G. Liu, *Laser Phys. Lett.* **2019**, *16*, 025103.

[15] J. Du, M. Zhang, Z. Guo, J. Chen, X. Zhu, G. Hu, P. Peng, Z. Zheng, H. Zhang, *Sci. Rep.* **2017**, *7*, 42357.

[16] Z.-C. Luo, M. Liu, Z.-N. Guo, X.-F. Jiang, A.-P. Luo, C.-J. Zhao, X.-F. Yu, W.-C. Xu, H. Zhang, *Opt. Express* **2015**, *23*, 20030.

[17] Z. Sun, H. Xie, S. Tang, X. F. Yu, Z. Guo, J. Shao, H. Zhang, H. Huang, H. Wang, P. K. Chu, *Angew. Chemie - Int. Ed.* **2015**, *54*, 11526.

[18] Z. Wang, Y. Xu, S. C. Dhanabalan, J. Sophia, C. Zhao, C. Xu, Y. Xiang, J. Li, H. Zhang, *IEEE Photonics J.* **2016**, *8*, 1.

[19] Y. Shi, H. Long, S. Liu, Y. H. Tsang, Q. Wen, *J. Mater. Chem. C* **2018**, *6*, 12638.

[20] H. Long, Y. Shi, Q. Wen, Y. H. Tsang, *J. Mater. Chem. C* **2019**, *7*, 5937.

[21] M. B. H. M. B. Hisyam, M. F. R. M. F. Rusdi, A. A. L. A. A. Latiff, and S. W. H. and S. W. Harun, *Chinese Opt. Lett.* **2016**, *14*, 081404.

[22] L. Yun, Y. Qiu, C. Yang, J. Xing, K. Yu, X. Xu, W. Wei, *Photonics Res.* **2018**, *6*, 1028.

[23] N. M. Radzi, A. A. Latif, M. F. Ismail, J. Y. C. Liew, E. Wang, H. K. Lee, N. Tamcheck, N. A. Awang, F. Ahmad, M. K. Halimah, H. Ahmad, *Results Phys.* **2020**, *16*, 103123.

[24] D. J. Lewis, P. Kevin, O. Bakr, C. A. Muryn, M. A. Malik, P. O'Brien, *Inorg. Chem. Front.* **2014**, *1*, 577.

[25] P. Reiss, M. Carrière, C. Lincheneau, L. Vaure, S. Tamang, *Chem. Rev.* **2016**, *116*, 10731.

[26] J. R. Brent, A. K. Ganguli, V. Kumar, D. J. Lewis, P. D. McNaughter, P. O'Brien, P. Sabherwal, A. A. Tedstone, *RSC Adv.* **2016**, *6*, 86955.

[27] A. Ishida, M. Aoki, and H. Fujiyasu, Semimetallic Hall properties of PbTe-SnTe superlattice, *J. Appl. Phys.*, **1985**, *58*, 1901.

[28] R. Rossetti, L. Brus, *J. Phys. Chem.* **1982**, *86*, 4470.

[29] P. K. Sarswat, S. Sarkar, G. Yi, M. L. Free, *J. Phys. Chem.C,* **2017**.

[30] D. Feng, Z. Ge, Y. Chen, J. Li, J. He, *Nanotechnology*, **2017**, *28*, *455707*.

[31] R. M. Kannaujiya, A. J. Khimani, S. H. Chaki, S. M. Chauhan, A. B. Hirpara, M. P. Deshpande, *Eur. Phys. J. Plus* **2020**, *123*, 1.

[32] S. G. Pandya, M. E. Kordesch, *Nanoscale Res. Lett.* **2015**, *10*, 0.

[33] Y. Wang, A. Hu, *J. Mater. Chem. C* **2014**, *2*, 6921.

[34] P. G. Luo, S. Sahu, S. T. Yang, S. K. Sonkar, J. Wang, H. Wang, G. E. Lecroy, L. Cao, Y. P. Sun, *J. Mater. Chem. B* **2013**, *1*, 2116.

[35] S. Khosravi, G. Bahram, K. Ramin, *J. Mater. Sci. Mater. Electron.* **2018**, *29*, 18989.

[36] M. E. Cryer, J. E. Halpert, *ACS Sensors* **2018**, *3*, 2087.

[37] J. Yang, W. Yu, Z. Pan, Q. Yu, Q. Yin, L. Guo, Y. Zhao, T. Sun, Q. Bao, K. Zhang, *Small* **2018**, *14*, 1.

[38] Z. Xie, F. Zhang, Z. Liang, T. Fan, Z. Li, X. Jiang, H. Chen, J. Li, H. Zhang, *Photonics Res.* **2019**, *7*, 494.

[39] A. S, A. M, D. K. and S. K. P. Sarkar, *npj 2D Mater. Appl.* **2020**,*4*, 1.

[40] Y. I. Jhon, J. Lee, M. Seo, J. H. Lee, Y. M. Jhon, *Adv. Opt. Mater.*, **2019**, *1801745*, 1.

[41] N. Yang, G. Zhao, J. S. Foord, *Nanocarbon Chemistry and Interfaces*, Wiley, Hoboken, NJ, USA, 2020.

[42] L. Zhao, J. Wang, J. Li, J. Liu, C. Wang, J. Wang, X. Wang, *Phys. Chem. Chem. Phys.* **2019**, *21*, 17978.

[43] U. B. Singh, D. Singh, S. Kumar, R. Dhar, M. B. Pandey, *J. Mol. Liq.* **2017**, *241*, 1009.

[44] N. Berchenko, R. Vitchev, M. Trzyna, R. Wojnarowska-Nowak, A. Szczerbakow, A. Badyla, J. Cebulski, T. Story, *Appl. Surf. Sci.* **2018**, *452*, 134.

[45] X. Zhang, H. Xie, Z. Liu, C. Tan, Z. Luo, H. Li, J. Lin, L. Sun, W. Chen, Z. Xu, L. Xie, W. Huang, H. Zhang, *Angew. Chemie - Int. Ed.* **2015**, *54*, 3653.

[46] O. D. Neikov, N. A. Yefimov, *Handbook of Non-Ferrous Metal Powders*, Elsevier, **2019**.

[47] P. K. Cheng, C. Y. Tang, X. Y. Wang, L.-H. Zeng, Y. H. Tsang, *Photonics Res.* **2020**, *8*, 511.

[48] R. Rosell, J. Gomez-Codina, C. Camps, J. A. Maestre, J. Padille, A. Cantó, J. L. Mate, S. Li, J. Roig, A. Olazábal, M. Canela, A. Ariza, Z. Skagel, J. Morera-Prat, A. Abad, *N. Engl. J. Med.* **1994**, *330*, 153.

[49] J. Qi, K. L. Wang, Y. M. Zhu, *J. Mater. Process. Technol.* **2003**, *139*, 273.

[50] M. A. Latina, S. A. Sibayan, D. H. Shin, R. J. Noecker, G. Marcellino, *Ophthalmology* **1998**, *105*, 2082.

[51] J. S. Liu, X. H. Li, Y. X. Guo, A. Qyyum, Z. J. Shi, T. C. Feng, Y. Zhang, C. X. Jiang, X. F. Liu, *Small* **2019**, *15*, 1.

[52] J. Feng, X. Li, Z. Shi, C. Zheng, X. Li, D. Leng, Y. Wang, J. Liu, L. Zhu, *Adv. Opt. Mater.* **2020**, *8*, 1.

[53] H. Zhang, P. Ma, M. Zhu, W. Zhang, G. Wang, S. Fu, *Nanophotonics* **2020**, 1.

[54] Z. Luo, M. Zhou, J. Weng, G. Huang, H. Xu, C. Ye, Z. Cai, *Opt. Lett.* **2010**, *35*, 3709.

[55] Y. Chen, G. Jiang, S. Chen, Z. Guo, X. Yu, C. Zhao, H. Zhang, Q. Bao, S. Wen, D. Tang, D. Fan, *Opt. Express* **2015**, *23*, 12823.

[56] K. Y. Lau, A. A. Latif, M. H. Abu Bakar, F. D. Muhammad, M. F. Omar, M. A. Mahdi, *Appl. Phys. B Lasers Opt.* **2017**, *123*, 1.

[57] X. Wang, P. K. Cheng, C. Y. Tang, H. Long, H. Yuan, L. Zeng, S. Ma, W. Qarony, Y. H. Tsang, *Opt. Express* **2018**, *26*, 13055.

[58] P. K. Cheng, C. Y. Tang, X. Y. Wang, L.-H. Zeng, Y. H. Tsang, *Photonics Res.* **2020**, *8*, 511.

[59] K. Niu, Q. Chen, R. Sun, B. Man, H. Zhang, *Opt. Mater. Express* **2017**, *7*, 3934.

[60] E. I. Ismail, N. A. A. Kadir, A. A. Latiff, H. Arof, S. W. Harun, *Opt. Quantum Electron.* **2019**, *51*, 1.

[61] N. M. Radzi, A. A. Latif, M. F. Ismail, J. Y. C. Liew, E. Wang, H. K. Lee, N. Tamcheck, N. A. Awang, F. Ahmad, M. K. Halimah, H. Ahmad, *Results Phys.* **2020**, *16*, 103123.

[62] H. Hassan, A. A. Salman, M. A. Munshid, A. Al-Janabi, *Opt. Fiber Technol.* **2019**, *52*, 101969.

[63] P. L. Huang, S.-C. Lin, C.-Y. Yeh, H.-H. Kuo, S.-H. Huang, G.-R. Lin, L.-J. Li, C.-Y. Su, W.-H. Cheng, *Opt. Express* **2012**, *20*, 2460.

[64] M. Liu, X.-W. Zheng, Y.-L. Qi, H. Liu, A.-P. Luo, Z.-C. Luo, W.-C. Xu, C.-J. Zhao, H. Zhang, *Opt. Express* **2014**, *22*, 22841.

[65] H. Long, C. Y. Tang, P. K. Cheng, X. Y. Wang, W. Qarony, Y. H. Tsang, *J. Light. Technol.* **2019**, *37*, 1174.

[66] Z. Xie, F. Zhang, Z. Liang, T. Fan, Z. Li, X. Jiang, H. Chen, J. Li, H. Zhang, *Photonics Res.* **2019**, *7*, 494.

[67] Y. I. Jhon, J. Lee, M. Seo, J. H. Lee, Y. M. Jhon, *Adv. Opt. Mater.* **2019**, *7*, 1.

[68] Y. I. Jhon, J. Koo, B. Anasori, M. Seo, J. H. Lee, Y. Gogotsi, Y. M. Jhon, *Adv. Mater.* **2017**, *29*, 1.

[69] J. Koo, Y. I. Jhon, J. Park, J. Lee, Y. M. Jhon, J. H. Lee, *Adv. Funct. Mater.* **2016**, *26*, 7454.

[70] N. Ming, S. Tao, W. Yang, Q. Chen, R. Sun, C. Wang, S. Wang, B. Man, H. Zhang, *Opt. Express* **2018**, *26*, 9017.

Figures and Tables:

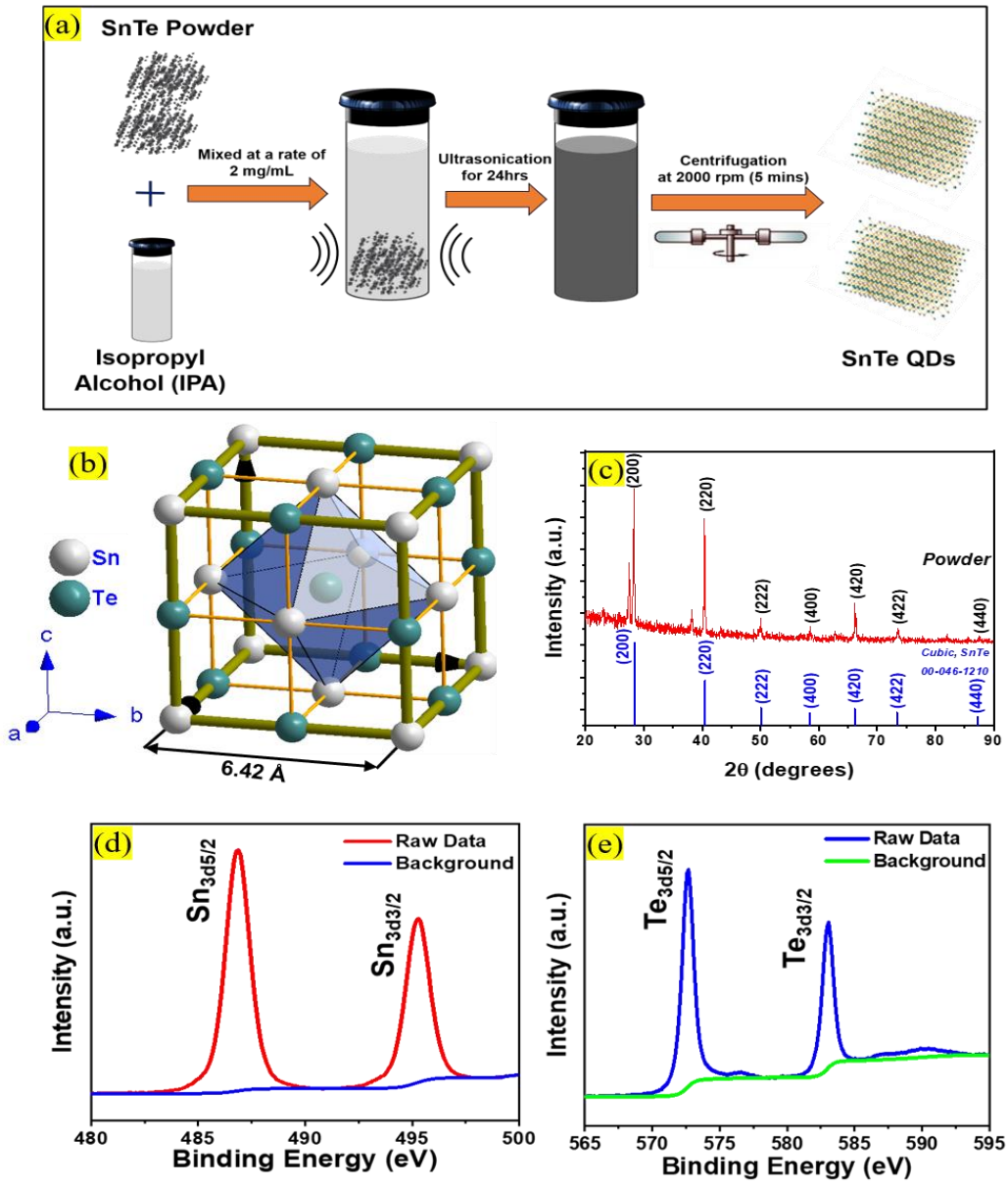

Figure 1. (a) Fabrication method of SnTe-QDs using LPE. (b) Rock salt crystal structure (FCC) of β-SnTe, where coordination octahedron is formed by each cation synchronized by six anions. (c) XRD pattern of SnTe-powder sample (top) and cubic SnTe (00-046-1210) stick pattern (bottom). High resolution X-ray photoelectron spectra (XPS) of (d) $Sn_{3d5/2}$, $Sn_{3d3/2}$ and (e) $Te_{3d5/2}$, $Te_{3d3/2}$.

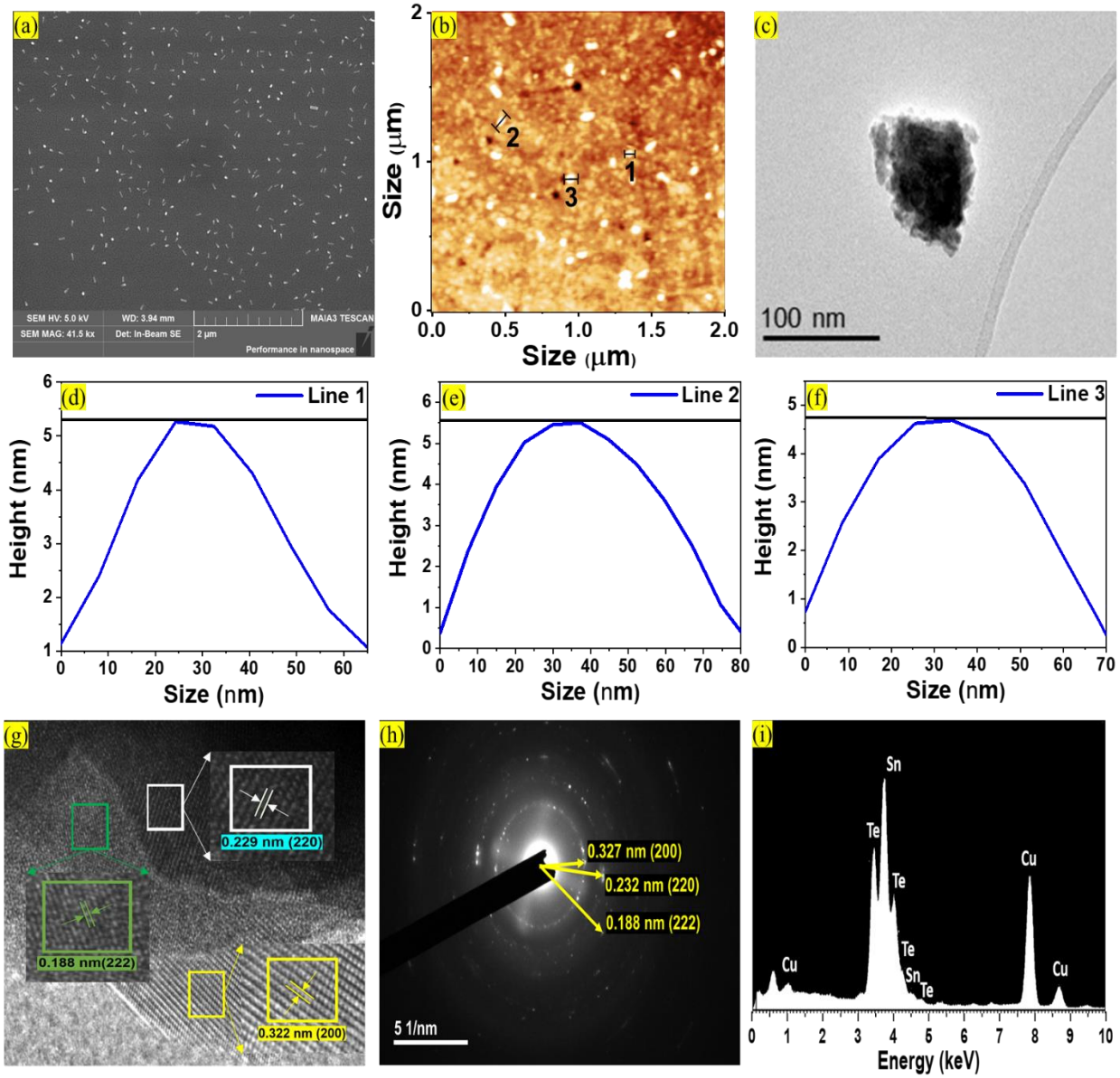

Figure 2. (a) FESEM image of SnTe-QDs. (b) AFM image; (d), (e), and (f) are the height profiles of line 1, 2 and 3 show in AFM image. (c) TEM image of the prepared sample at 30k magnification. (g) HRTEM image of a randomly selected SnTe-QDs, showing (200), (220) and (222) planes denoted by yellow, white, and green boxes, respectively. (h) SAED pattern and (i) EDS profile of SnTe QDs.

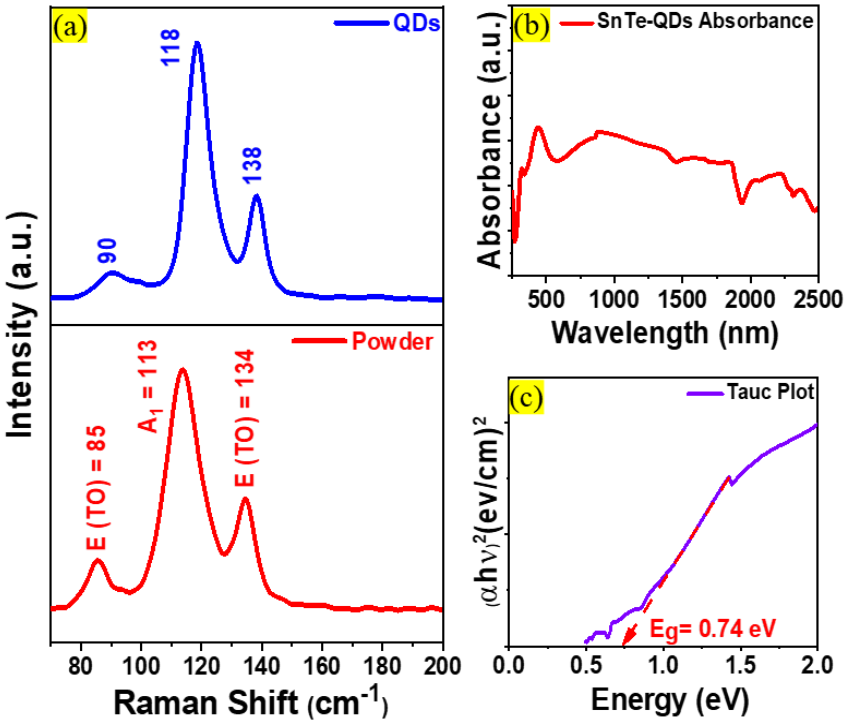

Figure 3. (a) Raman spectrum of SnTe powder (bottom) and QDs (top). (b) UV-vis-NIR optical absorption spectroscopy. (c) TAUC plot for defining bandgap of the SnTe-QDs.

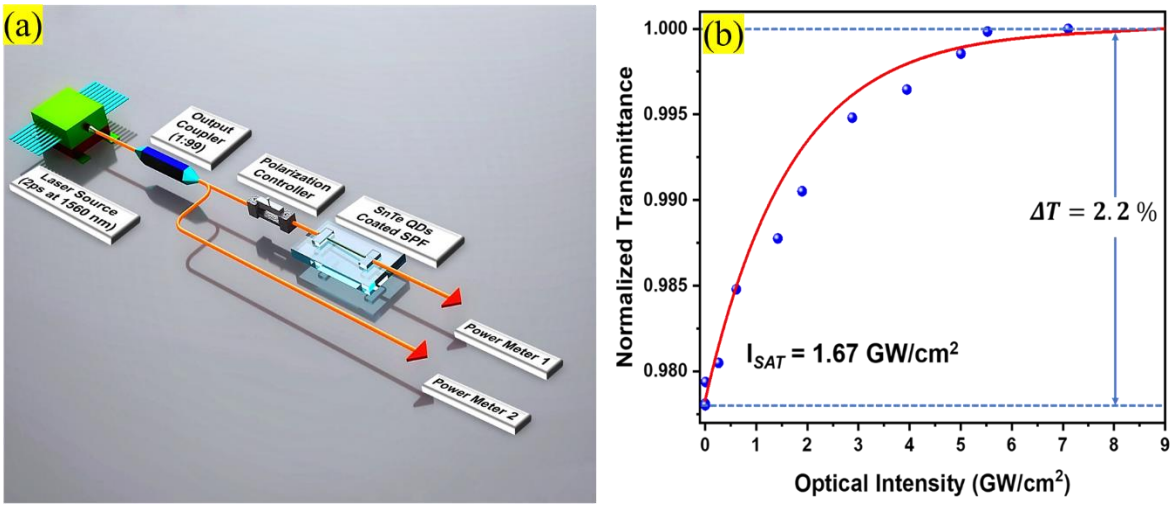

Figure 4. (a) The setup for the measurement of the saturable absorption curve of SnTe-QDs SA. (b) Nonlinear input intensity-dependent normalized transmittance curve of SnTe-QDs SA at 1564 nm.

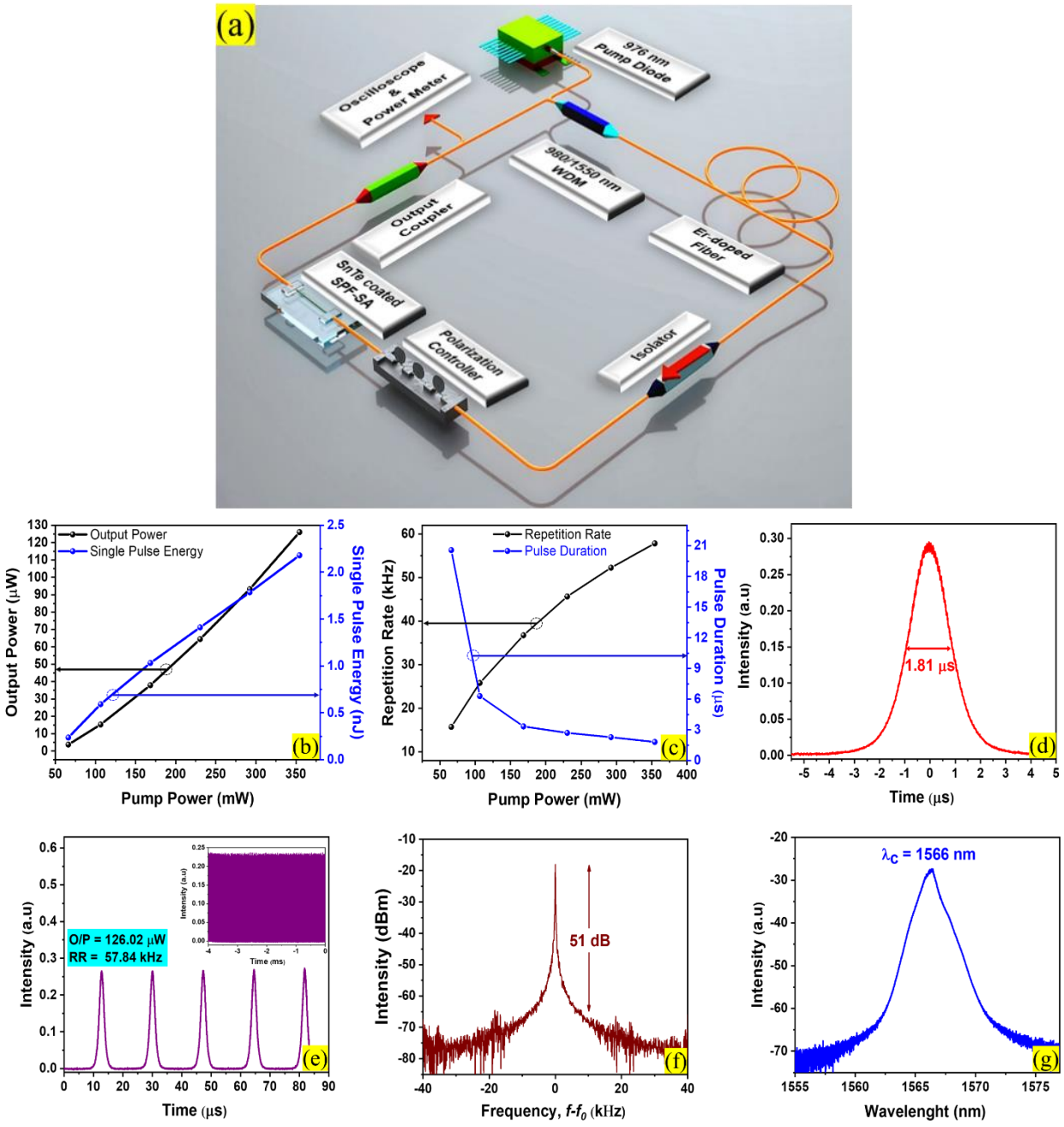

Figure 5. (a) Experimental schematic of the fiber laser system. Output characteristics of the Q-switching operation: (b) Output power and Single Pulse energy, and (c) Repetition rate and Pulse duration variation with respect to Pump Power. (d) Single-pulse profile for maximum pump power. (e) Pulse train at maximum pump power (inset is the large scale). (f) Observed RF spectrum. (g) Wavelength spectrum of the output pulse energy of 2.18 nJ.

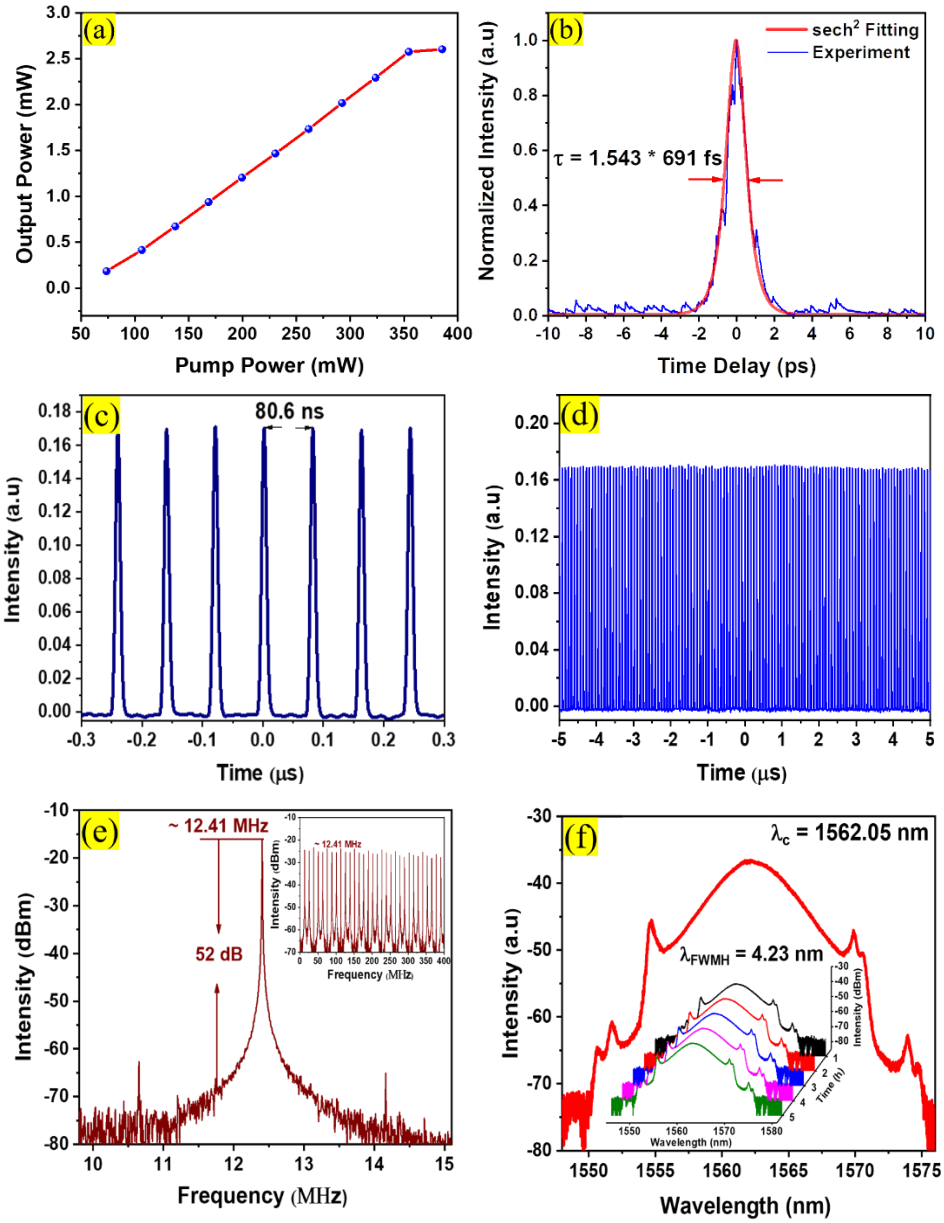

Figure 6. Output characteristics of the mode-locking operation: (a) Average output power evolution with respect to the pump power. (b) Mode-locked pulse width determined by auto-correlation trace; (c) & (d) Pulse train at different time scale; (e) Observed RF spectrum (inset is for broad scanning range); (f) Optical spectrum of the mode-locked pulse with 3 dB bandwidth of 4.23 nm at 1562.05 nm central wavelength (Inset is the wave spectrum obtained for 5 hours of operation).

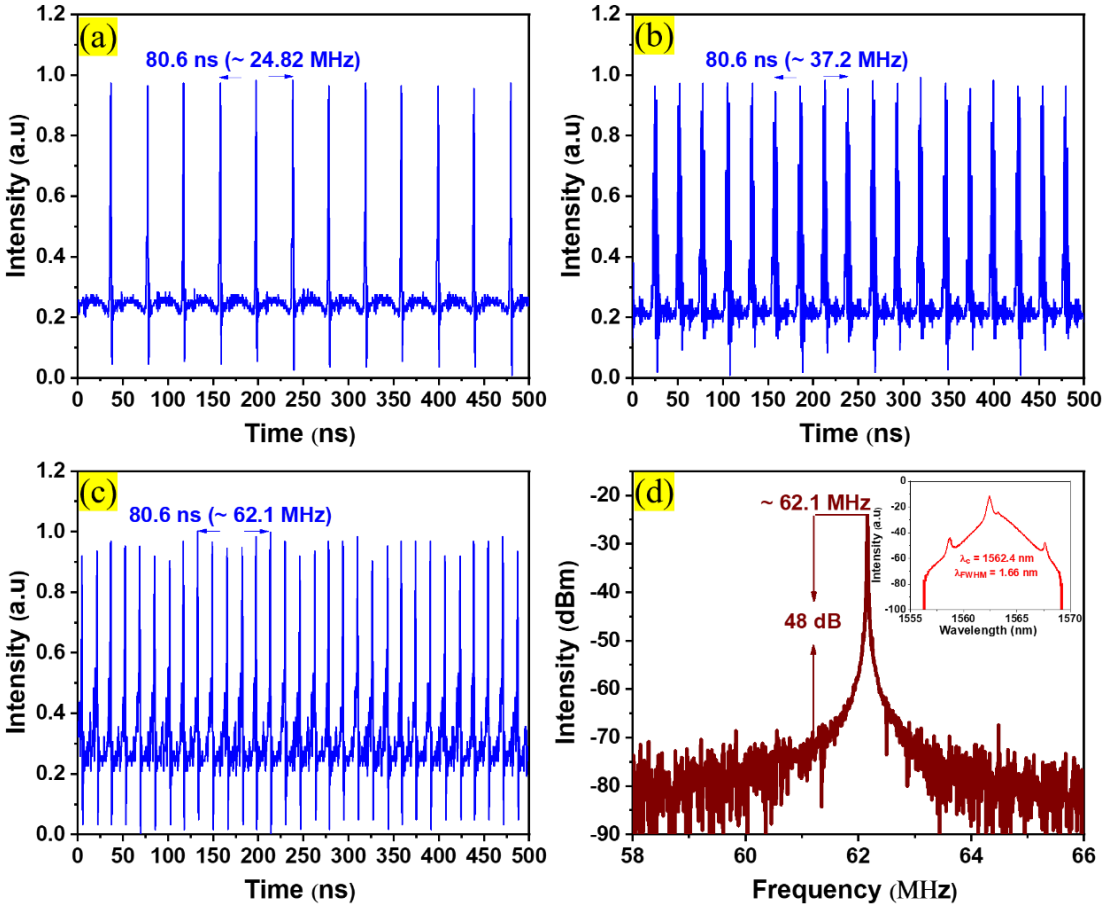

Figure 7. (a), (b) & (c) Pulse evaluations of 2nd, 3rd & 5th order of HML. (d) RF spectrum, and the optical spectrum (inset) of 5th order HML pulse.

Table 1. Comparisons of Q-switched lasers based on different SAs

	Material	Wavelength, nm (EDFL)	Pulse Duration, μs (SNR, dB)	Modulation Depth (%)	Pulse Energy (nJ)	References
Q-switching	Graphene	1566.35	3.7 (-)	-	16.7	[54]
	BP	1562.87	13.2 (45)	8.1	94.3	[55]
	MoS_2	1560	5.4 (-)	1.6	32.6	[13]
	WS_2	1560	2.6 (43.08)	4.1	120	[56]
	PtS_2	1569	4.2 (-)	-	45.6	[57]
	PdS_2	1567	4.5 (50)	1.7	15.1	[58]
	SnS_2	1532.7	510-1010 (50)	3.15	40.04	[59]
	CdSe-QDs	1559.35	4.30 (42)	-	11.83	[60]
	CdS-QDs	1562	1.27 (40)	19	50.8	[61]
	PbS-QDs	1533.04	3.5 (63)	1.15	121.2	[62]
	SnTe-QDs	**1566**	**1.81 (51)**	**2.17**	**2.18**	**This Work**

Table 2. Comparisons of Mode-locked lasers based on different SAs

	Material	Wavelength, nm (EDFL)	Pulse Duration, fs (SNR, dB)	Modulation Depth (%)	P_{output} (mW)	References
Mode-locking	Graphene	1559.1	432.47 (31)	2.93	2.29	[63]
	MoS_2	1556.86	3000	2.82	5.39	[64]
	PtS_2	1572	2060 (43)	7	1.1	[65]
	PdS_2	1565.8	803	1.7	0.55	[58]
	SnS	1560	656	36.4	1.1	[66]
	SnSe	1559	610	7.1	0.1	[67]
	MXene (Ti_3CN)	1550	660	1.7	0.05	[68]
	WTe_2	1556.2	770	2.85	0.04	[69]
	BPQDs	1568.5	1210 (61.3)	4.9	/	[18]
	Phosphorene QDs	1561.7	882 (67)	8.1	/	[15]
	PbS/CdS core/shell QDs	1562.5	5400 (50)	4.95	2.71	[70]
	$NbSe_2$ QDs	1556	756 (50)	3.72	8.5	[19]
	SnTe-QDs	**1562.6**	**691 (52)**	**2.17%**	**2.603**	**This Work**

Table of content

Tin Telluride Quantum Dots as a Novel Saturable Absorber

for Q-switching and Mode locking in fiber lasers

Safayet Ahmed [1,2,†], *Junpeng Qiao*[1,2,4†], *Ping Kwong Cheng*[1,2,†], *Ahmed Mortuza Saleque*[1,2],

Mohammad Ismail Hossain[1,2,3], *Long-Hui Zeng*[1,2], *Jia Zhao*[4],

Wayesh Qarony[1,2], *Yuen Hong Tsang*[1,2,*]

[1]Department of Applied Physics and Materials Research Center, The Hong Kong Polytechnic University, Hung Hom, Kowloon, Hong Kong

[2]Shenzhen Research Institute, The Hong Kong Polytechnic University, 518057 Shenzhen, Guangdong, People's Republic of China.

[3]Department of Materials Science and Engineering, City University of Hong Kong, Hong Kong

[4]School of Information Science and Engineering, Shandong University, Qingdao 266237, China

†Safayet Ahmed, Junpeng Qiao and Ping Kwong Cheng contributed equally to this work

*Corresponding author: E-mail: yuen.tsang@polyu.edu.hk

This is the first demonstration of fabricating Tin Telluride (SnTe)-Quantum Dots based saturable absorber, having average diameter of 74 nm (smaller than SnTe's Bohr Radius, 95 nm), via the liquid-phase exfoliation method. By utilizing it in a Er-doped fiber laser ring cavity system, Q-switched and mode-locked pulses with pulse width of 1.81 μs and 691 fs, respectively, along with 5th order Harmonic Mode locking with repetition rate of 62.1 MHz, are realized.

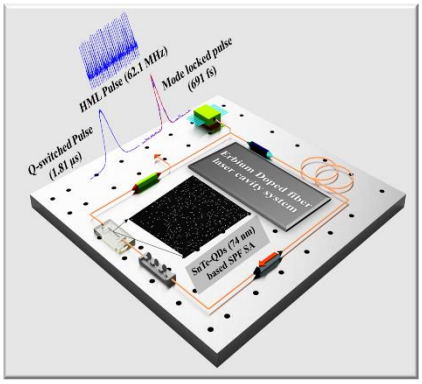

ToC figure

Supporting Informations

Tin Telluride Quantum Dots as a Novel Saturable Absorber for Q-switching and Mode locking in fiber lasers

Safayet Ahmed [1,2,†], Junpeng Qiao[1,2,4†], Ping Kwong Cheng[1,2,†], Ahmed Mortuza Saleque[1,2], Mohammad Ismail Hossain[1,2,3], Long-Hui Zeng[1,2], Jia Zhao[4], Wayesh Qarony[1,2], Yuen Hong Tsang[1,2,]*

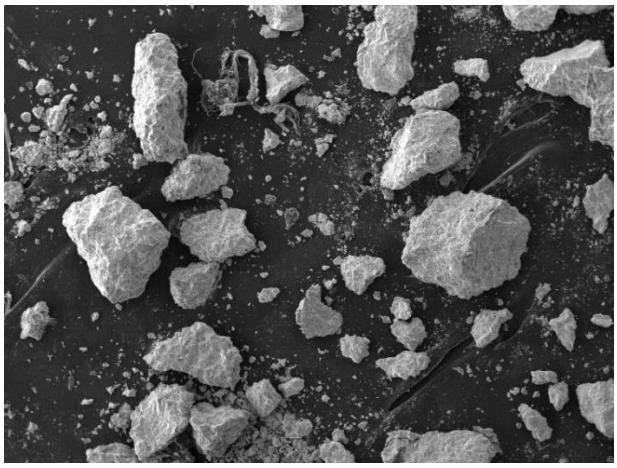

Figure S1. SEM image of the SnTe powder

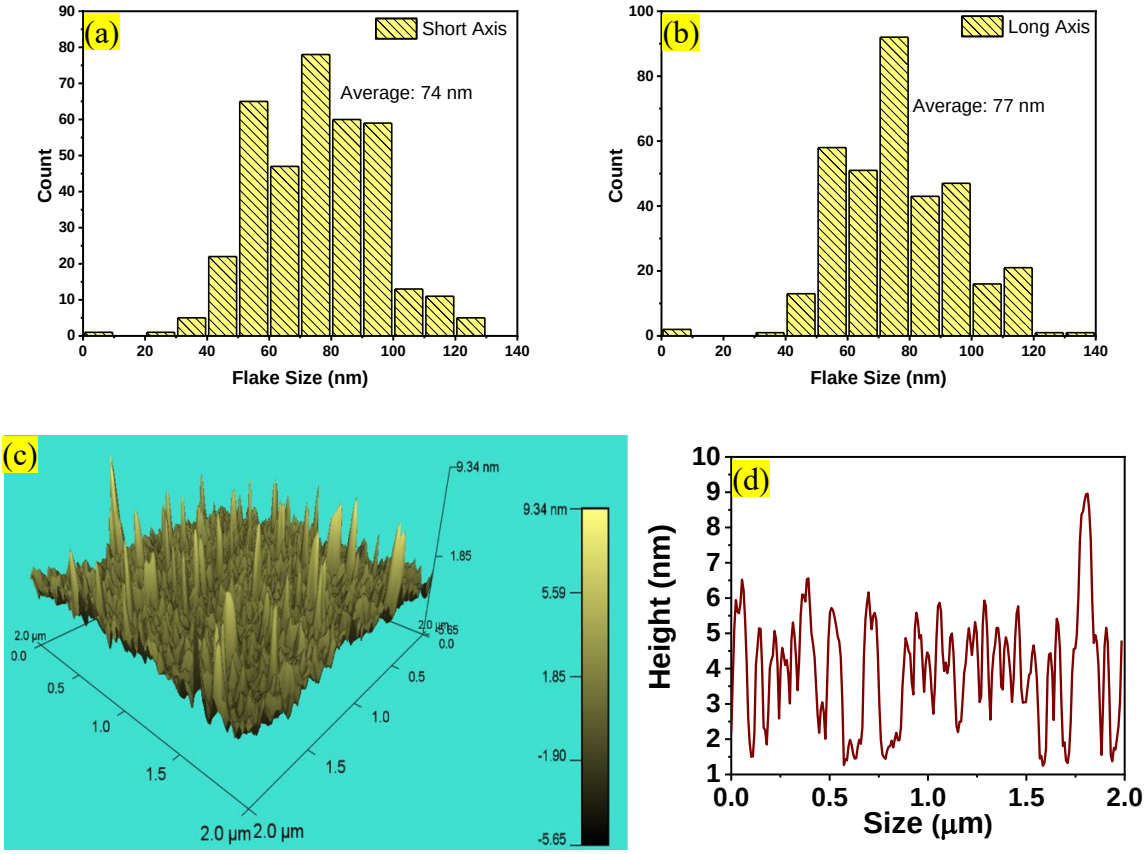

Figure S2. Statistical distribution of lateral size of the prepared SnTe-QDs along (a) short axis, and (b) long axis (analyzed from 369 QDs samples obtained from FESEM image); (c) and (d) 3D-AFM image and the height profile demonstrating the thickness of the prepared QDs.

Characterization of nonlinear optical properties

To determine nonlinear optical properties, a twin detector method is utilized, as shown in Figure 4(a). By using a homemade laser source (2.1 ps pulse width; center wavelength of 1560 nm, and pulse repetition rate of 15.04 MHz), a nonlinear saturable absorption curve was obtained. Here, an output coupler (1:99) was used to divide the laser output. A total of 99% output of the laser is passed through the SPF coated SnTe-QDs based saturable absorber, and the power is measured by a power meter (1). The 1% output was directly connected to another power meter (2). By comparing the values obtained from these two power meters, the transmittance value of the curve was determined. Thereafter, the transmittance value was normalized. To measure the optical intensity (GW/cm^2), we first determined the peak power, which was defined by the power meters. Subsequently, by dividing the peak power by the cavity RR (12.41 MHz), the single peak energy was calculated. Finally, the optical intensity was measured by dividing the single peak energy with the used laser sources' pulse width (2 ps) and area of the fiber core. For measuring the area, the diameter (d) of the fiber core was calculated to be 6 μm. Then, by fitting the curve with Equation 1, the value of the modulation depth (ΔT) and the saturable intensity (I_{sat}) were determined.

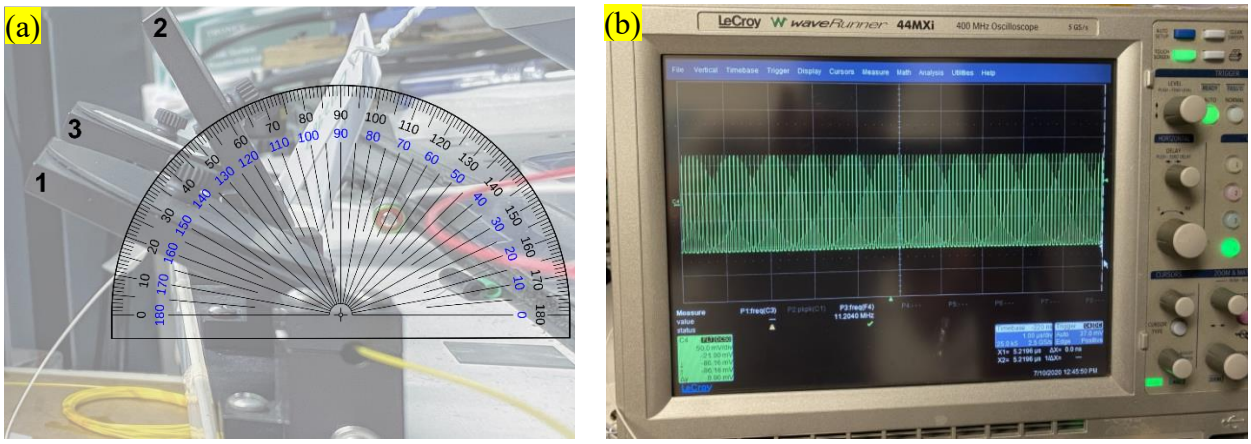

Figure S3. (a) Angle of the three paddles of Polarization controller during Mode locking operation; (b) Original oscilloscope view of the Mode-locking pulse train at pump power of 354 mW.

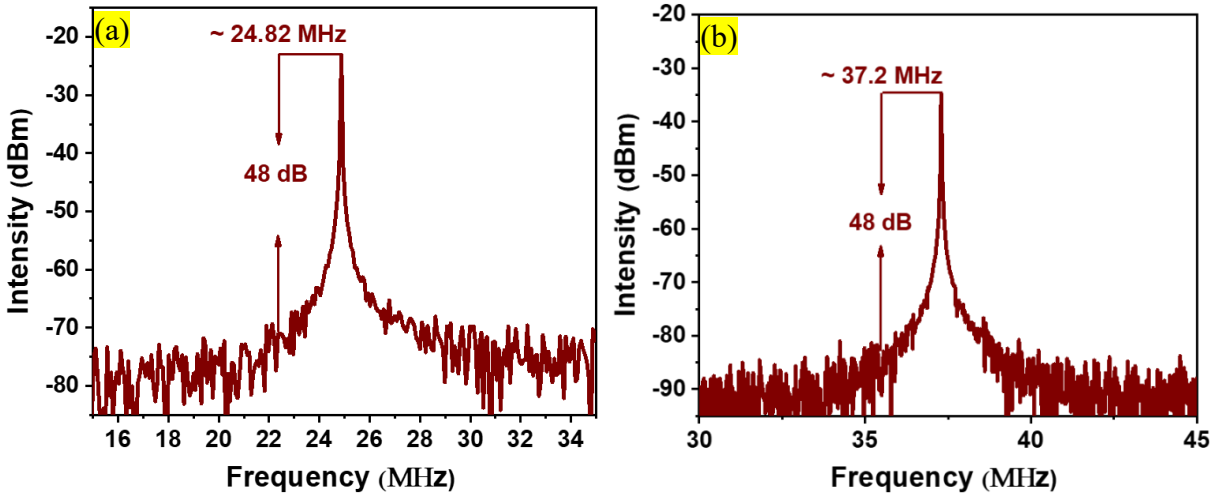

Figure S4. (a) and (b) RF spectrum of 2nd and 3rd order HML.

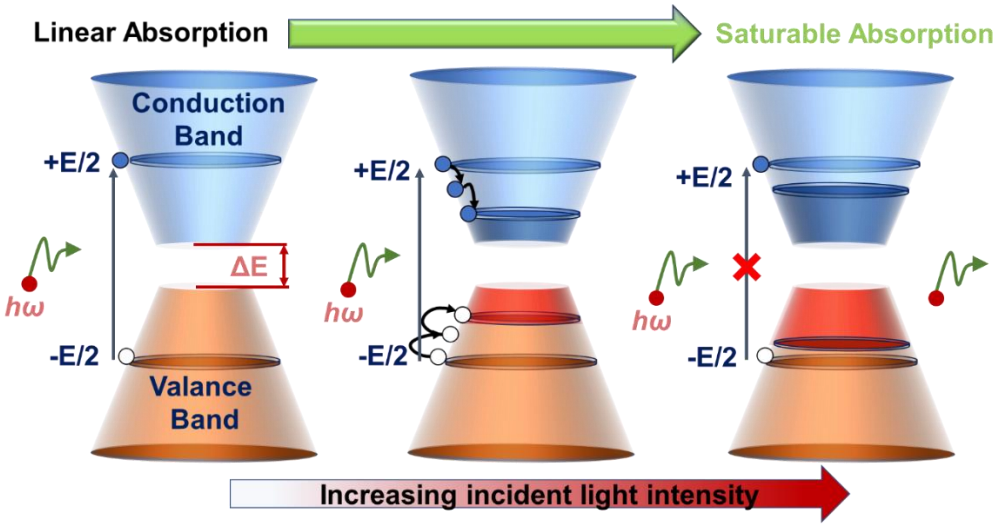

Figure S5. The saturable absorption mechanism of SnTe materials.